Chem. Res. Chinese Universities, 2020, 36(6), 1059—1067 doi: 10.1007/s40242-020-0278-9

Article

Boosting Photocatalytic Oxygen Evolution: Purposely Constructing Direct Z-Scheme Photoanode by Modulating the Interface Electric Field

LI Yinyin[1], WU Qiannan[2], ZHANG Kai[1], HU Bin[3], LIN Yanhong[1],
WANG Dejun[1] and XIE Tengfeng[1*]
1. Institute of Physical Chemistry, College of Chemistry, Jilin University, Changchun 130012, P. R. China;
2. State Key Laboratory of Inorganic Synthesis and Preparative Chemistry, College of Chemistry, Jilin University, Changchun 130012, P. R. China;
3. College of Chemistry, Jilin University, Changchun 130012, P. R. China

Abstract Ti-Fe_2O_3 photoanode has received widespread attention in photoelectrochemical(PEC) water spilling because of its optimized oxidative and reductive capability of composites catalyst. However, its low efficiency could limit its development. Herein, in order to improve the efficiency of PEC water spilling, the all-solid-state direct Z-scheme Ti-$ZnFe_2O_4$/Ti-Fe_2O_3(TZFO/Ti-Fe_2O_3) nanorod arrays composited with the ideal energy band structure are synthesized by modulating the Fermi level of TZFO for PEC water splitting. The photophysical methods in this work, including the Kelvin probe measurement and transient photovoltage spectroscopy(TPV) measurement, are applied to explore the migration behavior of electric charges at the enhanced interface electric field. Finally, the Z-scheme charge transfer mechanism of TZFO/Ti-Fe_2O_3 photoanode is proved successfully. Benefiting from the desirable charge transfer at interface electric field, the TZFO/Ti-Fe_2O_3 exhibits the outstanding photocatalytic oxygen evolution reaction(OER) performance, and the photocurrent of 60TZFO/Ti-Fe_2O_3 photoanode reaches 2.16 mA/cm^2 at 1.23 V *vs.* reversible hydrogen electrode(RHE), which is three times higher than that of pure Ti-Fe_2O_3 photoanode. This work provides a facile approach of modulating interface electric field to optimize the Z-scheme charge-transfer process.

Keywords Ti-$ZnFe_2O_3$/Ti-Fe_2O_3; Z-Scheme; Interface electric field; Heterojunction photoanode

1 Introduction

Photoelectrochemical(PEC) water splitting as a potential system for clean hydrogen energy has aroused more attention with the rapid consumption of fossil fuels[1,2]. Since TiO_2 was first reported as an effective photoelectrode for PEC water splitting by Fujishima *et al.*[3], growing research has been investigated to build the effective PEC materials. In fact, water oxidation determines the efficiency and performance of PEC water splitting, because it requires 4h$^+$ with consequent formation of O—O bond. Overall water splitting involves oxygen evolution reaction(OER)[Eq.(1)] and hydrogen evolution reaction(HER)[Eq.(2)] OER[4]:

$$2H_2O+4h^+ \longrightarrow O_2+4e^- \quad (1)$$

$$4H^++4e^- \longrightarrow 2H_2 \quad (2)$$

Therefore, exploring an excellent photoanode to improve the efficiency of water splitting becomes a key step in solving energy problems. So far, various photoelectrodes have been developed, such as $BiVO_4$[5], TiO_2[6], WO_3[7], ZnO[8], and α-Fe_2O_3 to improve the oxidation efficiency of water. Among them, n-type hematite(α-Fe_2O_3) has emerged as a promising photoanode material due to its excellent theoretical solar-to-hydrogen efficiency(15.8%), narrow bandgap and less toxic, but the pure α-Fe_2O_3 has poor photocatalytic activity owing to the short hole diffusion length, quick recombination of electron-hole pairs and sluggish oxygen evolution reaction(OER) kinetics[9—11]. Therefore, it is highly desired to explore more efficient α-Fe_2O_3-based photocatalysts to meet the requirement of practical application. Recently, direct Z-scheme photocatalytic systems formed by two semiconductors with the optimized oxidation and reduction capacity have attracted great attentions[12—15]. Taking ZnO-WO_{3-x} Z-scheme heterojunction as an example, this system is mainly attributed to its widened photoresponse range and effective carrier separation because of its special structure. As a result, the photo-generated charge by allowing the excited electron of ZnO recombining with the holes of WO_{3-x} leads to the accumulation of more holes in the surface of WO_{3-x} for the OER in water splitting[16]. Therefore, constructing α-Fe_2O_3-based Z-scheme heterojunction has been regarded as a very prospective approach to significantly improving the charge separation efficiency and optimizing the PEC water splitting performance[17]. Herein, the excited electron of α-Fe_2O_3 recombines with the holes of another semiconductor, thus, more holes transfer to the surface of

---

*Corresponding author. Email:xietf@jlu.edu.cn

Received September 1, 2020; accepted October 14, 2020.

Supported by the National Natural Science Foundation of China(Nos.51572106, 21773086, 21872063).

© Jilin University, The Editorial Department of Chemical Research in Chinese Universities and Springer-Verlag GmbH

α-Fe_2O_3 for the oxygen evolution reaction(OER) in PEC water splitting, accounting for high charge separation efficiency. In this regard, some research groups have built Z-scheme heterojunctions with α-Fe_2O_3, such as g-C_3N_4/α-Fe_2O_3[18], Fe_2O_3/Sb_2Se_3[19], CdS/Ti-Fe_2O_3[20], and these Z-scheme heterojunctions show the outstanding charge separation and lower recombination of electrons and holes in the bulk, resulting in an efficient PEC water splitting.

Typically, it is a challenge that how to prove the Z-scheme mechanism in heterojunction. Among them, many measurements have been proposed to prove the Z-scheme mechanism, such as photocatalytic-reduction testing[15], metal loading[21], X-ray photoelectron spectroscopy[22], and radical species trapping[23]. For example, the photo-deposition of metal NPs is widely applied to directly confirming the reduction site of photocatalytic system, thus providing information on the migration pathway of charge carriers. These examples provide the evidences why photo-generated carriers obey the Z-scheme migration mechanism for inducing spatial charge separation in photocatalysis. However, to date, most of the reported Z-scheme photocatalysts systems still suffer from the direct evidence to prove the migration of photo-generated charges at the interface electric field. According to our pervious report[24], the migration of electric charges at the interface electric field is critical for the investigation of Z-scheme heterojunctions. More importantly, the band bending of semiconductors triggered by interfacial electric fields is a promising way to explore the directional migration of charges at the interface electric field[25,26]. Therefore, precisely manipulating the interface of the heterojunctions based on SPV technology and TPV technology is an effective way to prove the Z-scheme migration mechanism.

In this study, we construct the Ti-$ZnFe_2O_4$/Ti-Fe_2O_3 (TZFO/Ti-Fe_2O_3) Z-scheme heterojunction photoanode as an example to manipulate the built-in electric field to explore the charge transfer path. Recently, $ZnFe_2O_4$(ZFO) has emerged as an outstanding photocatalytic material due to its stability in alkaline, narrow band gap(1.9 eV) and ideal band level[27—29]. With the matched band structure and Fermi level of α-Fe_2O_3, franklinite(ZFO) could be a good candidate to assemble Z-scheme heterojunction photoanode[30]. Herein, the built-in electric field of the ZFO/Ti-Fe_2O_3 heterojunction was tuned by precisely controlling the Fermi level of ZFO, which was realized by fabricating ZFO nanorods with different contents of Ti^{4+}. Particularly, due to the radius of Ti^{4+}(0.061 nm) being similar to that of the high spin Fe^{3+}(0.065 nm), Ti incorporation could lead that Ti^{4+} could take place of Fe^{3+} for a lattice contraction and a reduction in the unit cell volume of Fe_2O_3, leading to a lattice contraction and a reduction in the unit cell volume. In addition, Ti incorporation could lead to the enhanced outstanding charge carriers efficiency[31]. Hence, Ti stands out as a promising candidate for hematite doping to precisely control the Fermi level of ZFO. It is discovered that the PEC performance depends strongly on the interface barrier between TZFO and Ti-Fe_2O_3. Finally, the Z-scheme charge transfer mechanism of TZFO/Ti-Fe_2O_3 has been fully proved according to the results of WF measurement, SPV measurement, and TPV measurement. Herein, the holes on TZFO will combine with the electrons on Ti-Fe_2O_3, so that more holes on Ti-Fe_2O_3 can participate in the oxidation reaction of water splitting. More importantly, the Ti^{4+} doping amount in ZFO has been found to significantly modulate the Fermi level and further enhance the interface electric field of ZFO/Ti-Fe_2O_3. Accordingly, the best sample of 60TZFO/Ti-Fe_2O_3 shows the more outstanding PEC performance than pure Ti-Fe_2O_3 photoanode. In addition, the precise manipulation of the heterojunction interface provides an effective method for the exploration of the Z-scheme migration mechanism.

2 Experimental

2.1 Materials

All materials including ferric chloride hexahydrate ($FeCl_3\cdot6H_2O$; Alfa Aesar, 97.0%—102%), sodium nitrate ($NaNO_3$; Sinopharm Reagent), titanium tetrachloride($TiCl_4$; Sinoreagent Co., Ltd, 99.0%), $Zn(NO_3)_2$(Sinopharm Reagent) were used without further purification.

2.2 Synthesis of TZFO

ZFO nanorods were obtained by simple hydrothermal reaction according to the literature[32] with some modifications. It should be noted that the FTO glass was sonicated for 20 min in deionized water, ethanol, acetone, ethylacetate and ethanol successively before it was placed in the Teflon-lined autoclave. In brief, 0.0375 mol/L $FeCl_3\cdot6H_2O$, 0.025 mol/L $Zn(NO_3)_2\cdot6H_2O$ and 0.0375 mol/L $NaNO_3$ were dissolved in 20 mL of deionized water and stirred for 15 min to obtain the precursor solution. In order to optimize the PEC performances, 0.05% titanium tetrachloride($TiCl_4$) ethanol solution(volume fraction) in the aqueous solution was added to the precursor solution with different doping volume(45 μL, 60 μL, and 75 μL). According to different doping amounts, the materials were named ZFO, 45ZFO, 60ZFO and 75ZFO, respectively. Secondly, the clean FTO was placed into a Teflon lined stainless steel autoclave with conductive face facing down, and the precursor solution was transferred to a Teflon lined stainless steel autoclave for 5 h at 100 °C, then the autoclave was cooled down naturally. Then, the samples were cleaned with deionized water and dried in air, after that, the samples were placed in a muffle furnace annealing at 550 °C for 2 h at 2 °C/min and cooled to room temperature. Finally, because the ZFO nanorods were wrapped with an excess ZnO layer, this undesired ZnO skin was removed by soaking in a 1 mol/L KOH solution for 12 h.

2.3 Synthesis of TZFO/Ti-Fe_2O_3

The Ti-Fe_2O_3 nanorods arrays were synthesized on TZFO/FTO through a hydrothermal method reported previously[33,34]. The precursor solution has been prepared by dissolving 0.15 mol/L iron chloride hexahydrate($FeCl_3\cdot6H_2O$), 1 mol/L sodium nitrate($NaNO_3$), and 1 mL of 0.05% titanium tetrachloride($TiCl_4$) ethanol solution(volume fraction) in the aqueous solution.Then, the TZFO/FTO with its conductive side facing down the Teflon-lined autoclave was immersed in the above solution. Subsequently, the autoclave was transferred to an oven for 12 h, which was preadjusted to 100°C. The synthesized TZFO/Ti-Fe_2O_3 was annealed at 550 °C for 2 h under air atmosphere. According to the different doping amounts of ZFO, they were denoted as 45TZFO/Ti-Fe_2O_3, 60TZFO/Ti-Fe_2O_3, and 75TZFO/Ti-Fe_2O_3, respectively. The pure Ti-Fe_2O_3 was prepared by the same method.

2.4 Characterizations

The crystal structure and the phases of the photoanodes were analyzed using X-ray diffractionmethod(XRD, D/MAX2250 diffractometer) in the 2θ range from 10° to 80° at a scan rate of 10°/min. The surface morphology and film thickness were characterized using field-emission scanning electron microscopy(SEM, Hitachi Company) and high-resolution transmission electron microscopy(HRTEM, FEI Tecnai G2 F20). The surface chemical state of elements was evaluated by X-ray photoelectron spectroscopy(XPS) using the C1*s* peak as a correction. The UV-Vis absorption spectrum of the samples was obtained for the range of 300—800 nm by a UV-Vis-NIR spectrophotometer(Shimadzu UV-3600). The separation and kinetic behaviors of photogenerated charge carriers were studied with the aid of lock-in-based SPV measurement and TPV measurement. The WF measurement was carried out on a Kelvin probe instrument(SKP 5050, KP Technology Ltd., UK).

2.5 PEC Measurements

All PEC measurements were explored under a 300 W xenon lamp(PLS-SXE300, Perfectlight) simulated AM 1.5G illumination(100 mW/cm^2) from the photoanode side with an electrochemical station(CHI 660E) in a standard three-electrode configuration, consisting of the prepared photoanodes, Pt, and Ag/AgCl as the working electrode, counter electrode, and reference electrode, respectively. The applied potential *versus* Ag/AgCl was translated into potential *versus* RHE on the basis of the Nernst equation[Eq.(3)]:

$$E_{\mathrm{RHE}} = E_{\mathrm{Ag/AgCl}} + 0.059\mathrm{pH} + E^{\theta}_{\mathrm{Ag/AgCl}} \tag{3}$$

The electrolyte in our PEC measurements was 1 mol/L KOH(pH=13.8) unless otherwise specified, and the active area was 0.283 cm^2. The current *vs*. potential curve was obtained by linear sweep voltammetry(LSV) at a scan rate of 10 mV/s. Applied bias photon to current efficiency(E_{ABPE}) was calculated *via* the Eq.(4):

$$E_{\mathrm{ABPE}} = (J_{\mathrm{light}}–J_{\mathrm{dark}}) \times (1.23–V_{\mathrm{RHE}})/P_{\mathrm{light}} \tag{4}$$

where J_{light} and J_{dark} refer to the current densities of the synthesized photoanodes under illumination and in dark, respectively. V_{RHE} refers to the applied potential *versus* RHE, and P_{light} refers to the incident light intensity(100 mW/cm^2). The accumulated charge densities of the TZFO/Ti-Fe_2O_3 film were obtained by integrating the transient photocurrent density at different potential values from 0.8 V to 1.6 V(*vs*. RHE). The injection efficiencies of the photoanodes were obtained through employing 0.5 mol/L H_2O_2 as a hole scavenger in 1 mol/L KOH electrolyte, the oxidation of H_2O_2 is more favorable thermodynamically and kinetically than water. The injection efficiency(η_{inj}) was determined by using Eq.(5):

$$\eta_{\mathrm{inj}}= J_{\mathrm{H_2O}}/J_{\mathrm{H_2O_2}} \tag{5}$$

where $J_{\mathrm{H_2O}}$ and $J_{\mathrm{H_2O_2}}$ refer to the photocurrent densities for PEC H_2O oxidation and PEC H_2O_2 oxidation, respectively. The separation efficiency of photogenerated charge carriers during reaction was characterized by the difference values of open circuit potential between dark and illumination. The EIS was measured with a frequency range of 105 Hz to 0.05 Hz at 1.0 V *vs*. RHE under illumination(100 mW/cm^2) to ascertain the charge transport of the photoanode. In addition, incident photon to current conversion efficiency(IPCE) was carried out at 1.23 V *vs*. RHE with the help of a monochromator, and the intensity of monochromatic light was measured by a calibrated Si photodiode. IPCE was obtained according to the Eq.(6):

$$\mathrm{IPCE}=\frac{J\times1240}{P_{\mathrm{mono}}\times\lambda} \tag{6}$$

3 Results and Discussion

3.1 Characterization

The X-ray diffraction(XRD) pattern is conducted to determine the crystal structure of the obtained photoanode. The significant peak of 35.63° also corresponds to (311) facet of pure $ZnFe_2O_4$ phase(JCPDS No. 73-1963) in Fig.S1(A)(see the Electronic Supplementary Material of this paper), indicating the successful preparation of ZFO. Furthermore, the XRD patterns of TZFO with different Ti doping amounts have no obvious change, because the Ti doping amount is too small to be detected. In addition, it is evident that all the diffraction peaks of TZFO/Ti-Fe_2O_3 could be indexed to Ti-Fe_2O_3 (PDF#33-0664), ZFO and FTO in Fig.S1(B)(see the Electronic Supplementary Material of this paper)[35]. The morphologies of the Ti-Fe_2O_3 and TZFO/Ti-Fe_2O_3 are characterized by SEM and HRTEM, respectively. Fig.1(A) shows the pure Ti-Fe_2O_3 photoanode nanorods with a diameter of *ca*. 60 nm are aligned vertically to the FTO substrate. Besides, the surface and morphology of the 60TZFO/Ti-$Fe_2O_3$are similar to those of the pure Ti-Fe_2O_3 in Fig.1(B), and the only change is that its size increases slightlywith the diameter of 75 nm because the 60TZFO/Ti-Fe_2O_3 nanorods are a combination of TZFO nanorods and Ti-Fe_2O_3 nanorods. In addition, the pristine 60TZFO exhibits nanorods with a diameter of 38 nm in Fig.S2(see the Electronic Supplementary Material of this paper). This further proves indirectly the successful introduction of TZFO.

The HRTEM image of 60TZFO/Ti-Fe_2O_3 displays the interplanar spacing of 0.22 nm in Fig.2(A), which is indexed to

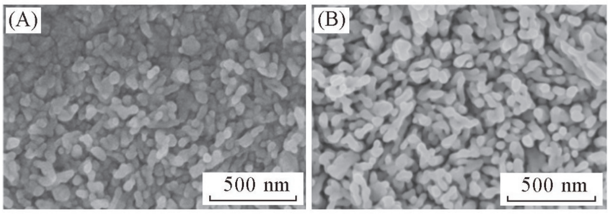

Fig.1 Top-view SEM images of Ti-Fe_2O_3(A) and 60TZFO/Ti-Fe_2O_3(B)

(113) planar of Ti-Fe_2O_3. Another interplanar spacing of 0.252 nm obtained from the inner nanorods belongs to the (311) plane of $ZnFe_2O_4$. HRTEM image demonstrates the 60TZFO/Ti-Fe_2O_3 heterojunction photoanode has been successfully synthesized. In addition, energy-dispersive X-ray spectroscopy (EDS) elemental mapping illustrates the existence and uniform distribution of Fe, O, Zn and Ti element in 60TZFO/Ti-Fe_2O_3 as shown in Fig.2(B).

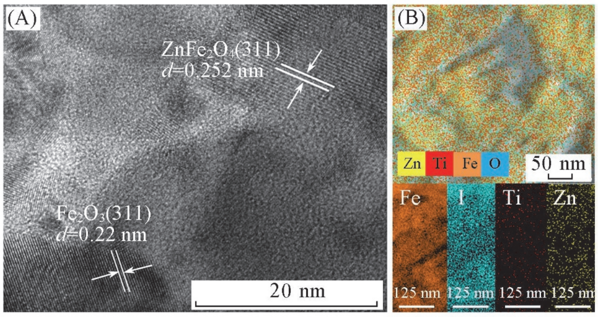

Fig.2 HRTEM image of 60TZFO/Ti-Fe_2O_3(A) and EDS elemental mappings of Fe, O, Ti and Zn of 60ZFO/Ti-Fe_2O_3(B)

The XPS is used to further determine the valence and chemical composition of 60TZFO/Ti-Fe_2O_3. The survey spectrum demonstrates the coexistence of Fe, O and Ti elements. Fig.3(A) shows three peaks at 710.12, 724.75 and 718.91 eV in the Fe_{2p} XPS spectrum, corresponding to $Fe_{2p_{3/2}}$ and$Fe_{2p_{1/2}}$ and Fe^{3+} severally. The O_{1s} spectrum in Fig.3(B) shows that two peaks are attributed to the chemisorbed O and lattice O, respectively. In addition, Fig.S3(see the Electronic Supplementary Material of this paper) manifests that the peak of Ti_{2p} at 458.1 eV is assigned to Ti^{4+} in 60TZFO/Ti-Fe_2O_3 photoanode.

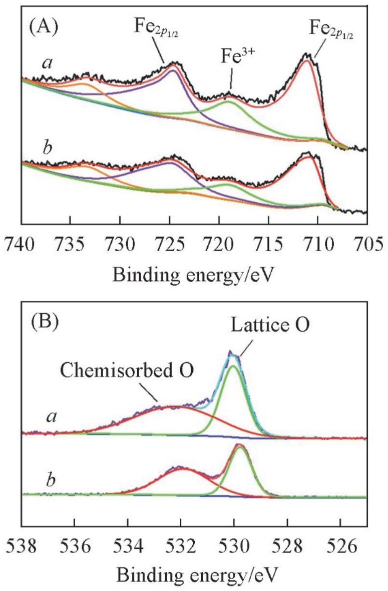

Fig.3 XPS spectra of Fe_{2p}(A) and O_{1s}(B) from 60TZFO/Ti-Fe_2O_3(*a*) and TZFO(*b*), respectively

The UV-Vis diffuse reflection absorption spectra of pure Ti-Fe_2O_3 and TZFO/Ti-Fe_2O_3 film are shown in Fig.S4(A)(see the Electronic Supplementary Material of this paper). After the introduction of TZFO, the absorption range of the photoanode has no change significantly. In order to determine whether the TZFO has an effect on the band gap of Ti-Fe_2O_3, the band gaps obtained by Tauc's plots of the absorption curves are shown in Fig.S4(B)(see the Electronic Supplementary Material of this paper). From Fig.S4, we can find that there is no obvious change for TZFO/Ti-Fe_2O_3 compared with the pure Ti-Fe_2O_3 in the absorption edge. Therefore, light absorption is not the main reason for the catalytic performance.

3.2 PEC Performance of TZFO/Ti-Fe_2O_3 Electrodes

Fig.4(A) shows the current density-potential curves of Ti-Fe_2O_3 and TZFO/Ti-Fe_2O_3 photoanodes under AM 1.5G simulated sunlight, It is obvious that the TZFO/Ti-Fe_2O_3 has the more excellent photocurrent compared with the pure Ti-Fe_2O_3, especially for the sample of 60TZFO/Ti-Fe_2O_3. Fig.4(B) shows the photocurrent density of 60TZFO/Ti-Fe_2O_3 reaches 2.16 mA/cm^2 at 1.23 V *vs*. RHE, which is three times higher than that of pure Ti-Fe_2O_3. In addition, the incident photocurrent conversion efficiency(IPCE) at 1.23 V *vs*. RHE was measured to understand the relationship between the PEC activity and the wavelength of the incident light. Fig.4(C) shows that the 60TZFO/Ti-Fe_2O_3 photoanodes show the more intensive IPCE values from 370 nm to 560 nm compared with the pure Ti-Fe_2O_3, suggesting the fast charge separation and rapid electron transport of Ti-Fe_2O_3 after introducing TZFO, for the enhancement of the solar energy conversion efficiency[36]. In addition, the maximum applied bias photon-to-current efficiency(ABPE) value of 60TZFO/Ti-Fe_2O_3 was 0.13% at 1.1 V *vs*. RHE in Fig.4(D), which is 2.2 times higher than that of pure Ti-Fe_2O_3(0.06% at 1.11 V *vs*. RHE).

In order to probe the influence of the enhanced separation transfer of photoinduced charge carriers on PEC performance, the open-circuit photovoltage(OCPV) calculated was carried out from the difference of open-circuit potentials between dark and illumination in 1 mol/L KOH. As shown in Fig.5(A), the samples of TZFO/Ti-Fe_2O_3have the higher OCPV values in comparison with Ti-Fe_2O_3, and the sample of 60TZFO/Ti-Fe_2O_3 has the highest OCPV value, indicating the charge separation efficiency is improved when we introduced TZFO in the Ti-Fe_2O_3. In addition, Fig.5(B) shows that the injection efficiencies of TZFO/Ti-Fe_2O_3 are enhanced compared with the pure Ti-Fe_2O_3. Herein, the carrier-injection efficiency of 60TZFO/Ti-Fe_2O_3 Z-scheme heterojunction photoanode was about 44%, which is 2.4 times higher than that(18%) for pure Ti-Fe_2O_3 at 1.23 V *vs*. RHE.These results demonstrated that more holes migrate to the surface of Ti-Fe_2O_3 for water splitting reaction, suggesting that the introduction of TZFO could account for the reducing of the recombination probability of photo-generated charges and the accumulation of more holes on the surface to participate in PEC water splitting. In addition, the 60TZFO/Ti-Fe_2O_3 Z-scheme heterojunction photoanode delivers the most obvious photo-responses to light on/off switching as compared to other photoanode in Fig.5(C). Moreimportantly, 60TZFO/Ti-Fe_2O_3 can maintain about 96% of theinitial photocurrent density after 2 h photostability measurement as shown

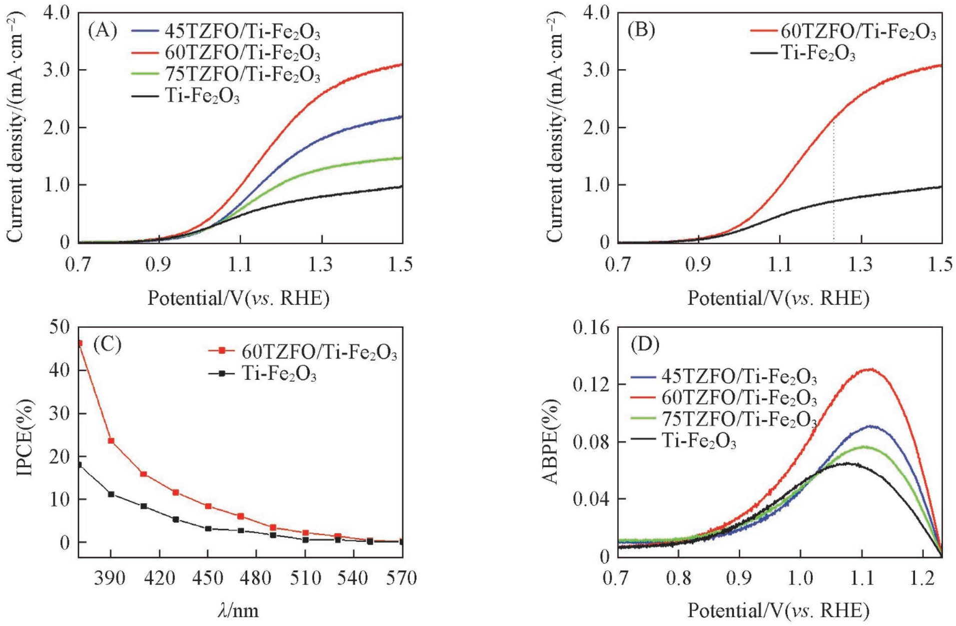

Fig.4 Current density-potential curves of Ti-Fe_2O_3, TZFO/Ti-Fe_2O_3(A), and Ti-Fe_2O_3, 60TZFO/ Ti-Fe_2O_3(B), IPCE plots of Ti-Fe_2O_3 and 60TZFO/Ti-Fe_2O_3 at 1.23 V *vs*. RHE(C) and applied bias photon-to-current efficiencies(ABPE) of Ti-Fe_2O_3 and TZFO/Ti-Fe_2O_3(D)

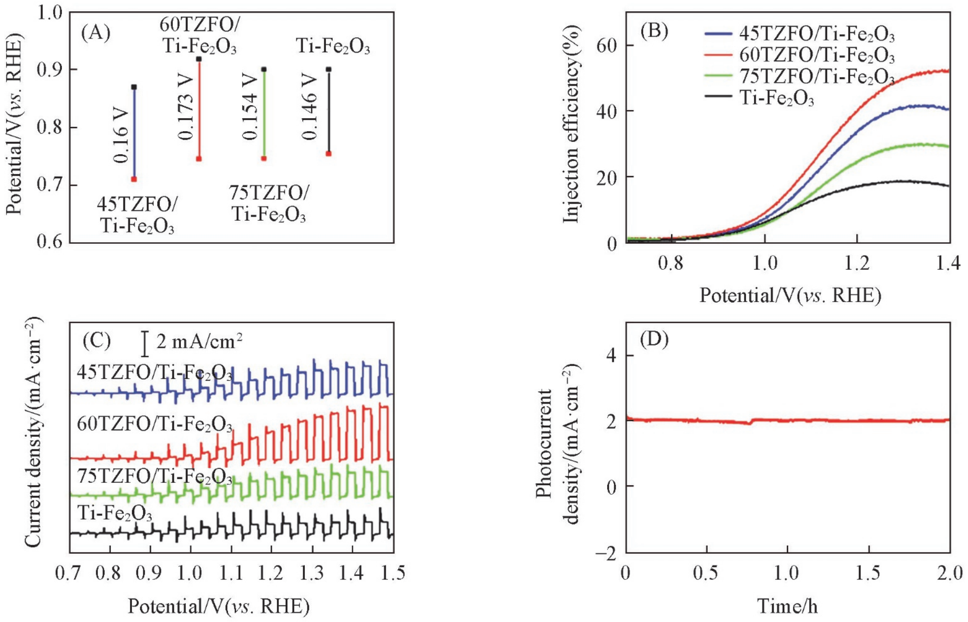

Fig.5 Opencircuit potentials(OCPV) of Ti-Fe_2O_3 and TZFO/Ti-Fe_2O_3 electrodes measured in the dark(red) and under illumination(black) in 1 mol/L KOH electrolyte(A), injection efficiencies of Ti-Fe_2O_3 and TZFO/ Ti-Fe_2O_3 photoanode(B), currentpotential curves of Ti-Fe_2O_3 and TZFO/Ti-Fe_2O_3 under chopped light(C) and the PEC OER stability test of 60TZFO/Ti-Fe_2O_3 photoanode at 1.23 V *vs*. RHE(D)

in Fig.5(D), indicating its photostability for PEC water splitting reaction. The above results confirmthat the important role of ZFO on promoting the PEC water splitting performance of TZFO/Ti-Fe_2O_3 Z-scheme photoanode, and the construction of Z-scheme photoanode promotes the charge transport and separation at the interface between TZFO and Ti-Fe_2O_3. However, it is not clear whether the introduction of TZFO will promote the migration of charges at the interface. Therefore, the exploration of the interface electric field is the key step to reveal the improvement of PEC performance.

To further investigate charge transfer between the TZFO and the Ti-Fe_2O_3 interface, we conduct EIS test to obtain the Nyquist plots of Ti-Fe_2O_3 and TZFO at 1.0 V *vs*. RHE under AM 1.5 G illumination. It should be noted that the semicircles at high frequency region represent the charge transfer in the bulk photoanode and the semicircles at low frequency region are related to the charge transfer process at the photoanode/ electrolyte interface. Fig.6(A) shows the radii of two semicircles for TZFO/Ti-Fe_2O_3 decrease remarkably compared with that of pure Ti-Fe_2O_3, especially the 60TZFO/Ti-Fe_2O_3 has the smallest radii compared with other photoanodes, indicating the smallest charge transfer resistance in the bulk photoanode and at the photoanode/electrolyte interface when introducing 60TZFO. In order to further analyze the charge transfer process, Nyquist plots are fitted to an equivalent circuit as shown in Fig.6(B) and the fitting results list in Table S1(see the Electronic Supplementary Material of this paper). Herein, R_1 is related to the charge transfer resistance in bulk photoanodes, whereas R_2corresponds to the transport resistance at the interface of photoanodes and electrolyte. As a result, 60TZFO/Ti-Fe_2O_3 displays the smallest R_1 than other modified electrodes, indicating the lowest charge transport resistance and the highest charge transfer efficiency in the bulk. In addition, the reducedR_2 data of photoanodes when introducing TZFO exhibit the decreased transfer resistance at the Ti-Fe_2O_3 and electrolyte interface, leading that more holes will migrate to the surface of Ti-Fe_2O_3. These results indicate that the introduction of TZFO is conducive to improve the interfacial charge transfer kinetics and optimize the PEC performance.

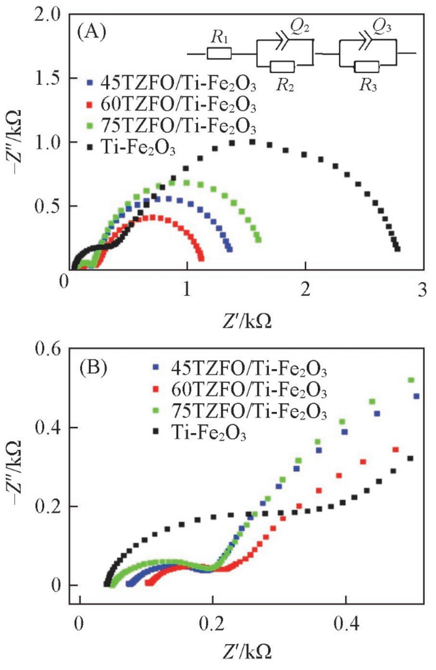

Fig.6 Nyquist plots of Ti-Fe_2O_3 and TZFO/Ti-Fe_2O_3 photoanode at 1.0 V *vs*. RHE under AM 1.5G illumination(the inset is the equivalent circuit diagram)(A) and high-frequency zone enlarged version(B)

3.3 Separation and Transfer of Photogenerated Charge Carriers of TZFO/Ti-Fe_2O_3

Water oxidation on photoanodes proceeds through three steps: light absorption, transport of the photogenerated charge carriers, and charge transfer at the solid-liquid interface to oxidize water[37]. According to the previous analysis about UV-Vis diffuse reflection absorption spectra of pure Ti-Fe_2O_3 and TZFO/Ti-Fe_2O_3, we can conclude that the light absorption is not the main reason for the catalytic performance. Besides, there also has no obvious change of surface morphology for the comparison of TZFO/Ti-Fe_2O_3 and Ti-Fe_2O_3 according to SEM results, so the charge transfer at the solid-liquid interface is not the main reason for the catalytic performance. Therefore, we suppose that transport of the photo-generated charge carriers is the main factor for the improvement of the PEC performance without co-catalyst loading. Herein, we adopted SPV measurement and TPV measurement to explore the separation efficiency of the photoanodes. According to our pervious report[38,39], the SPV and TPV signals could be used to analyze the surface charge behavior of photoanodes when illuminated from the FTO electrode side, and thepositive signal represents that the holes transfer to the surface and thenegative signal represents the migration of electrons to the surface.

The SPV spectra of 60TZFO/Ti-Fe_2O_3 heterojunction and Ti-Fe_2O_3 films are obtained in Fig.7(A) under the front side illumination(the monochromatic light irradiated from FTO electrode side) condition. In this way, most of the photons are absorbed at the Ti-Fe_2O_3 layer, and the photoinduced charge carriers are separated by the effect of interfacial electric field. As a result, we can see a positive SPV response during the whole response range, which indicates that photoinduced holes transfer to the irradiation side under the action of interfacial electric field. Besides, the stronger the positive signal, the higher the efficiency of charge separation. In addition, the conventional TPV signal of the Ti-Fe_2O_3 and TZFO/Ti-Fe_2O_3 electrodes under 355 nm laser pulse waw explored to further research the separation efficiency of the photoanodes in Fig.7(B). Obviously, the 60TZFO/Ti-Fe_2O_3 photoanode has the strongest positive signal than other photoanode, meaning the highest separation efficiency compared with other samples. This resultis consistent with the SPV result. Therefore, the

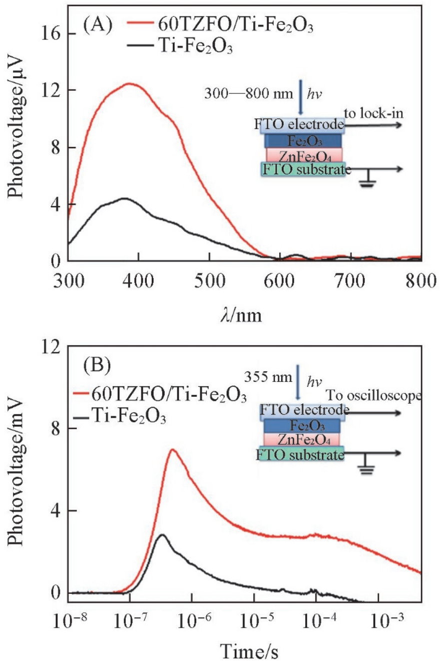

Fig.7 SPV signal of Ti-Fe_2O_3 and 60TZFO/Ti-Fe_2O_3 photoanode(A) and TPV signal of Ti-Fe_2O_3 and 60TZFO/Ti-Fe_2O_3 photoanode(B)

(A) The inset shows the schematic of SPV measurements; (B) the inset shows the schematic of TPV measurements.

built-in electricfield at TZFO/Ti-Fe_2O_3 interface favors the photoexcited electron transfer to TZFO and more photoexcited holes transfer to Ti-Fe_2O_3 for PEC water splitting.

3.4 Z-Scheme Charge Transfer Mechanism

The above results confirm that the structure of TZFO/Ti-Fe_2O_3 shows higher charge-separation efficiency than Ti-Fe_2O_3. In order to further analyze the reason for the enhancement of charge-separation efficiency, the study of the interface charge migration behavior between TZFO and Ti-Fe_2O_3 is carried out. Herein, we assume that TZFO and Ti-Fe_2O_3 formed Z-scheme heterojunction photonodes, and in this Z-scheme system, the electrons on Ti-Fe_2O_3 with a lower conduction band potential could combine with the holes on TZFO with a higher valence band potential, leading to the accumulation of more holes at the surface of Ti-Fe_2O_3 for the OER in water splitting. Based on this assumption, we investigate the built-in electric field at TZFO/Ti-Fe_2O_3interface by the Work Function(WF) measurement. The WF(Φ) of the TZFO and Ti-Fe_2O_3 was tested through the Kelvin probe technique, which indirectly reveals the contact potential difference(CPD) between the samples and the Au probe. The WF values of $ZnFe_2O_4$ and Ti-Fe_2O_3 are calculated according to the following equation:

$$\Phi_{\text{sample}}=\Phi_{\text{Au}}+eCPD(\Phi_{\text{Au}}=4.9\ \text{eV}) \tag{7}$$

In this work, the built-in electric field of the ZFO/Ti-Fe_2O_3 heterojunction is tuned by precisely controlling different contents of Ti^{4+} in TZFO, and then adjusting the Fermi level of ZFO. As shown in Fig.S5(A)(see the Electronic Supplementary Material of this paper), the CPDs values of the Ti-Fe_2O_3 and $ZnFe_2O_4$ are –160 and –223 mV, respectively. Therefore, the WF values of $ZnFe_2O_4$ and Ti-Fe_2O_3 are 4.667 and 4.74 eV based on the Eq.(4), and these data indicate that the Fermi level of $ZnFe_2O_4$ is higher than that of Ti-Fe_2O_3. Hence, $ZnFe_2O_4$ could form an upward bend while Ti-Fe_2O_3 could form a downward bend when they contact, which is beneficial for the electrons transfer from Ti-Fe_2O_3 to $ZnFe_2O_4$. Obviously, it is reasonable that the holes of $ZnFe_2O_4$ combine with the electrons of Ti-Fe_2O_3, leading that more holes of Ti-Fe_2O_3 migrate to the surface for PEC water splitting. Generally, the charge transfer behavior of heterojunction between two semiconductors depends on the interface band bending, which is further determined by their band structures and Fermi levels. Fig.S5(B) shows that as the work function value of $ZnFe_2O_4$ decreases, the electric field at the interface between $ZnFe_2O_4$ and Ti-Fe_2O_3 gradually strengthens. If the TZFO/Ti-Fe_2O_3 photoanodes are transferred by typical type-II, it will become more difficult to transfer electrons from ZFTO to Ti-Fe_2O_3 due to the increasing interface barrier, leading to the reduced charge transfer efficiency. The above results confirm that the structure of TZFO/Ti-Fe_2O_3 shows higher charge-separation efficiency than Ti-Fe_2O_3, therefore, TZFO/Ti-Fe_2O_3 photoanodes are not the typical type-II composite, and its interfacial charge transfer behavior will follow the Z-scheme route for the improvement of the charge-separation efficiency.

To further ascertain the Z-scheme charge transfer mechanism of TZFO/Ti-Fe_2O_3, the interfacial charge transfer behavior of TZFO/Ti-Fe_2O_3 could also be studied by transient photovoltaic technology(TPV). For the present work, the conventional TPV signal of the Ti-Fe_2O_3 and TZFO/Ti-Fe_2O_3 electrodes is explored to research the superficial charge transfer behavior when sample is illuminated from the sample side under 532 nm laser pulse. Theoretically, the more positive signal suggests that more holes could transfer to the surface of Ti-Fe_2O_3. As shown in Fig.8(A), the TZFO/Ti-Fe_2O_3 photoanodes show a more positive signal than the pure Ti-Fe_2O_3, which means that more electrons migrate to the surface of the Ti-Fe_2O_3 to recombine with the holes of the TZFO, thereby weakening the recombination of bulk electrons and holes of the Ti-Fe_2O_3. In addition, the TPV signals can explain the charge transfer process under the interface electric field when the sample is illuminated from the FTO substrate side[34]. Therefore, the TPV measurement of 60TZFO/Ti-Fe_2O_3 photoanode is further conducted to study the charge transfer behavior at interface electric field when illuminating from TZFO side as shown in Fig.8(B). Compared to Ti-Fe_2O_3, the reduced positive signal indicates that more electrons have migrated to the illuminated side(TZFO side) in a short time(10^{-8}—10^{-5} s), and the decreasing positive photovoltage signal can be seen for TZFO electrode in a short time, which implies that TZFO photoanode generates smaller Schöttky barrier under the influence of TZFO during the electron transmission process, and the smoother electron transfer process in TZFO/Ti-Fe_2O_3 compared to Ti-Fe_2O_3. More importantly, for TZFO/Ti-Fe_2O_3 photoanode, its TPV spectrum shows a negative response in a long time(10^{-5}—0.01 s), which indicates that photoinduced electrons transfer to the illuminated side under the action of interfacial electric field. Specifically, for the spatial charge separation in the TZFO/Ti-Fe_2O_3

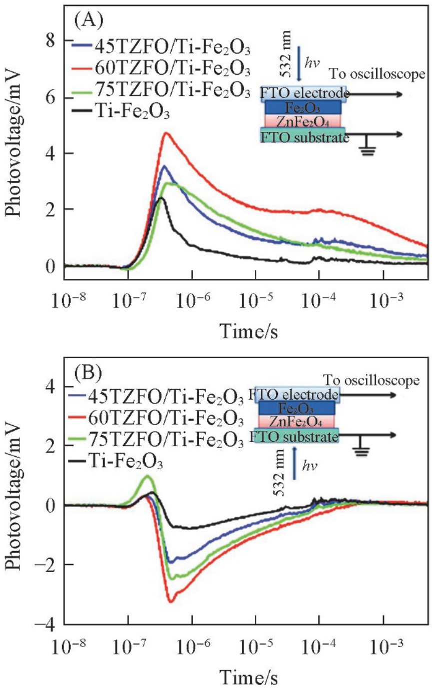

Fig.8 TPV signal of Ti-Fe_2O_3 and TZFO/Ti-Fe_2O_3 photoanode when illuminating from Ti-Fe_2O_3 side(A) and from TZFO side(B)

photoanode induced by the built-in electric field at the interface, photogenerated holes transfer from TZFO to Ti-Fe_2O_3, and more photogenerated electrons migrate from TZFO to FTO side, leading to a more negative signal in TZFO/Ti-Fe_2O_3 than that in pure Ti-Fe_2O_3. Therefore, the results of TPV indicate that the behavior of electron transfer is from Ti-Fe_2O_3 to TZFO driven by the formation of the interface electric field, which is consistent with the result of Work Function(WF) measurement and the TZFO/Ti-Fe_2O_3 photoanode will follow the Z-scheme electron transfer mechanism.

According to the above analysis, the schematic band diagram of TZFO/Ti-Fe_2O_3 based on Z-scheme charge transfermechanism is proposed in Scheme 1. As TZFO and Ti-Fe_2O_3 contact to form the heterojunction, the recombination of photogenerated electrons from Ti-Fe_2O_3 with the photogenerated holes on TZFO could promote the photogenerated electron-holes separation efficiency of Ti-Fe_2O_3, optimizing the oxidation potential of this photocatalytic system, and enhancing its PEC performance.

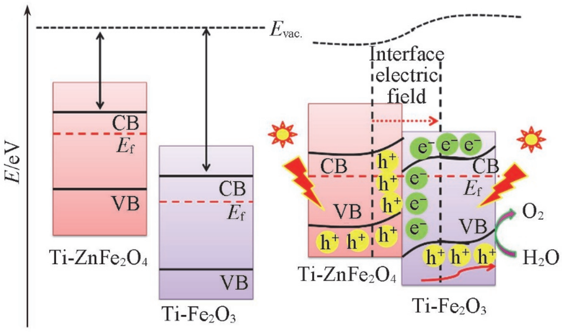

Scheme 1 Schematic band diagram of TZFO/Ti-Fe_2O_3

4 Conclusions

In summary, the direct Z-scheme TZFO/Ti-Fe_2O_3 nanorod arrays with the suitable band structures and Fermi levels were constructed by two step hydrothermal treatment for PEC water splitting. Herein, the built-in electric field of the ZFO/Ti-Fe_2O_3 heterojunction was tuned by precisely controlling the Fermi level of ZFO, and the charge migration behavior at the interface proves that the TZFO/Ti-Fe_2O_3 heterojunction photoanode obeys the Z-scheme mechanism, thereby eliminating the possibility of type II heterojunction. In addition, the Z-scheme charge transfer mechanism of TZFO/Ti-Fe_2O_3can be successfully explored through the Kelvin probe measurement, SPV measurement and TPV measurement. As a result, TZFO/Ti-Fe_2O_3Z-scheme heterojunction photoanodes exhibit outstanding PEC performance in water splitting, and the photocurrent of 60TZFO/Ti-Fe_2O_3 photoanode reaches 2.16 mA/cm^2 at 1.23V *vs*. RHE, which is three times higher than that of pure Ti-Fe_2O_3 photoanode. The improved PEC performance could be attributed to the excellent separation efficiency at interfacial electric field, and the Z-scheme heterojunction photoanode can greatly enhance the utilization of the photogenerated holes with high oxidation abilities. This work provides an effective strategy to prove the Z-scheme migration mechanism by precisely tuning the fermi level.

Electronic Supplementary Material

Supplementary material is available in the online version of this article at http://dx.doi.org/10.1007/s40242-020-0278-9.

References

[1] Li J., Zhan G., Yu Y., Zhang L., *Nat.Commun.*, **2016**, *7*, 11480
[2] Ran J., Zhang J., Yu J., Jaroniec M., Qiao S. Z., *Chem. Soc. Rev.*, **2014**, *43*, 7787
[3] Fujishima A., Honda K., *Nature*, **1972**, *238*, 37
[4] Le Formal F., Pendlebury S. R., Cornuz M., Tilley S. D., Gratzel M., Durrant J. R., *J. Am. Chem. Soc.*, **2014**, *136*, 2564
[5] Kölbach M., Harbauer K., Ellmer K.,van de Krol R., *J. Phys. Chem. C*, **2020**, *124*, 4438
[6] Chen Y., Ji S., Sun W., Lei Y., Wang Q., Li A., Chen W., Zhou G., Zhang Z., Wang Y., Zheng L., Zhang Q., Gu L., Han X., Wang D., Li Y., *Angew. Chem. Int. Ed.*, **2020**, *59*, 1295
[7] Jadwiszczak M., Jakubow-Piotrowska K., Kedzierzawski P., Bienkowski K., Augustynski J., *Adv. Energy Mater.*, **2019**, *10*, 1903213
[8] Dong X., Yang P., Wang J., Huang B., *ChemPlusChem*, **2014**, *79*, 1681
[9] Chen D., Liu Z., Zhang S., *Appl. Catal. B*, **2020**, *265*, 118580
[10] Lim H., Kim J. Y., Evans E. J., Rai A., Kim J. H., Wygant B. R., Mullins C. B., *ACS Appl. Mater. Inter.*, **2017**, *9*, 30654
[11] Yi S. S., Wulan B. R., Yan J. M., Jiang Q., *Adv. Funct. Mater.,* **2019**, *29*, 1801902
[12] Bakr A. E. A., El Rouby W. M. A., Khan M. D., Farghali A. A., Xulu B., Revaprasadu N., *Solar Energy*, **2019**, *193*, 403
[13] Low J., Dai B., Tong T., Jiang C., Yu J., *Adv. Mater.*, **2019**, *31*, 1802981
[14] Wang S., Zhu B., Liu M., Zhang L., Yu J., Zhou M., *Appl. Catal. B*, **2019**, *243*, 19
[15] Jiang W., Zong X., An L., Hua S., Miao X., Luan S., Wen Y., Tao F. F., Sun Z., *ACS Catal.*, **2018**, *8*, 2209
[16] Chen Y., Wang L., Gao R., Zhang Y. C., Pan L., Huang C., Liu K., Chang X. Y., Zhang X., Zou J. J., *Appl. Catal. B*, **2019**, *259*, 118079
[17] Low J., Jiang C., Cheng B., Wageh S., Al-Ghamdi A. A., Yu J., *Small Methods*, **2017**, *1*, 1700080
[18] Jiang Z., Wan W., Li H., Yuan S., Zhao H., Wong P. K., *Adv. Mater.*, **2018**, *30*, 1706108
[19] Liao A., Zhou Y., Xiao L., Zhang C., Wu C., Asiri A. M., Xiao M., Zou Z., *Nanoscale*, **2018**, *11*, 109
[20] Shen R., Zhang L., Chen X., Jaroniec M., Li N., Li X., *Appl. Catal. B*, **2020**, *266*, 118619
[21] Xu F., Xiao W., Cheng B., Yu J., *Int. J. Hydrogen Energ.*, **2014**, *39*,

15394

[22] Yu W., Xu D., Peng T., *J. Mater. Chem. A*, **2015**, *3*, 19936

[23] Liu Y., Chen Y., Zhou W., Jiang B., Zhang X., Tian G., *Catal. Sci. Technol.*, **2018**, *8*, 5535

[24] Zhang R., Bi L., Wang D., Lin Y., Zou X., Xie T., Li Z., *J. Colloid. Interf. Sci.*, **2020**, *578*, 431

[25] Weidner M., Fuchs A., Bayer T. J. M., Rachut K., Schnell P., Deyu G. K., Klein A., *Adv. Funct. Mater.*, **2019**, *29*, 1807906

[26] Sun H., Neumann C., Zhang T., Loffler M., Wolf A., Hou Y., Turchanin A., Zhang J., Feng X., *Adv. Mater.*, **2019**, *31*, 1900961

[27] Rong X., Chen H., Rong J., Zhang X., Wei J., Liu S., Zhou X., Xu J., Qiu F., Wu Z., *Chem. Eur. J.*, **2019**, *371*, 286

[28] Guo Y., Zhang N., Wang X., Qian Q., Zhang S., Li Z., Zou Z., *J. Mater. Chem. A*, **2017**, *5*, 7571

[29] Rawal S. B., Kang H. J., Won D. I., Lee W. I., *Appl. Catal. B*, **2019**, *256*, 117856

[30] McDonald K. J., Choi K. S., *Chem. Mater.*, **2011**, *23*, 4863

[31] Feng F., Li C., Jian J., Li F., Xu Y., Wang H., Jia L., *Journal of Power Sources*, **2020**, 449

[32] Lan Y., Liu Z., Guo Z., Ruan M., Xin Y., *J. Colloid. Interf. Sci.*, **2019**, *552*, 111

[33] Bu Q., Li S., Wu Q., Bi L., Lin Y., Wang D., Zou X., Xie T., *ChemSusChem*, **2018**, *11*, 3486

[34] Wu Q., Bu Q., Li S., Lin Y., Zou X., Wang D., Xie T., *J. Alloy. Compd.*, **2019**, *803*, 1105

[35] Bu Q., Li S., Wu Q., Lin Y., Wang D., Zou X., Xie T., *Catal. Sci. Technol.*, **2019**, *9*, 5812

[36] Liu J., Li J., Shao M., Wei M., *J. Mater. Chem. A*, **2019**, *7*, 6327

[37] Lee J. M., Baek J. H., Gill T. M., Shi X., Lee S., Cho I. S., Jung H. S., Zheng X., *J. Mater. Chem. A*, **2019**, *7*, 9019

[38] Jiang T., Xie T., Chen L., Fu Z., Wang D., *Nanoscale*, **2013**, *5*, 2938

[39] Jiang T., Xie T., Yang W., Chen L., Fan H., Wang D., *J. Phys. Chem. C*, **2013**, *117*, 4619